ENGINEERING

Imperceptible magnetic sensor matrix system integrated with organic driver and amplifier circuits

M. Kondo[1,2,3], M. Melzer[4]*, D. Karnaushenko[4], T. Uemura[1,3], S. Yoshimoto[1], M. Akiyama[1], Y. Noda[1], T. Araki[1,2,3], O. G. Schmidt[4,5,6†], T. Sekitani[1,2,3†]

Artificial electronic skins (e-skins) comprise an integrated matrix of flexible devices arranged on a soft, reconfigurable surface. These sensors must perceive physical interaction spaces between external objects and robots or humans. Among various types of sensors, flexible magnetic sensors and the matrix configuration are preferable for such position sensing. However, sensor matrices must efficiently map the magnetic field with real-time encoding of the positions and motions of magnetic objects. This paper reports an ultrathin magnetic sensor matrix system comprising a 2 × 4 array of magnetoresistance sensors, a bootstrap organic shift register driving the sensor matrix, and organic signal amplifiers integrated within a single imperceptible platform. The system demonstrates high magnetic sensitivity owing to the use of organic amplifiers. Moreover, the shift register enabled real-time mapping of 2D magnetic field distribution.

INTRODUCTION

Over the past decade, the development of flexible sensor systems, such as those for sensing pressure (*1*), temperature (*2*, *3*), strain (*4*, *5*), and biological potential (*6*), has attracted increased research attention owing to prospective utilization in applications such as robotics (*7*), electronic skins (e-skins) (*8*), and future bio-integrated consumer electronics (*9*). These applications rely heavily on the use of motile interacting objects and often involve operations performed on inconsistently shaped surfaces. Therefore, the integration of sensors capable of reliably providing information on relative positions, distances, and motion of interacting parts of a flexible electronic system is of critical importance. Among various sensors, magnetic field sensors have been typically used to perform these tasks, thereby triggering recent developments in flexible magnetic sensors (*10*–*14*) introduced in line with notable advancements in the field of flexible electronics (*15*, *16*). Flexible magnetic sensors are suitable for use in position control systems used in applications such as development of soft robots (*7*), wearable electronics (*1*, *2*) and smart textiles (*17*), contactless human-machine interfaces (*12*), and triggering systems (*12*), as well as nondestructive material testing in industries (*18*).

The development of state-of-the-art, flexible (*19*, *20*), and imperceptible (*16*, *21*) electronic sensors—directly created on thin and ultrathin polymer membranes—has also been recently reported, demonstrating their diverse functionalities along with characteristics of high surface compliance, wear-proof structure, and low specific weight. However, despite substantial progress in the development of imperceptible electronic devices, only very few studies have investigated advanced flexible magnetic systems capable of integrating individual magnetic sensors and other electronic devices (*22*).

The electronic devices that should be specifically integrated in a flexible magnetic system are active-matrix driver and signal amplifier circuits. To facilitate real-time capturing of spatially distributed physical quantities, most applications require many sensors to be distributed over large free-surface areas. Numerous sensors organized in an array require deployment of an efficient on-site sensor-scanning mechanism to avoid excessive interconnections (*1*, *16*), which, in turn, cause unacceptable compromises to be made in terms of array dimensions and reliability. In conventional electronic devices, the commutation of each array element to the external readout circuitry is driven by active-matrix drivers—complex circuits usually incorporated within rigid silicon dies. In large electronic devices, such as displays and sensor arrays, a separate matrix driver addresses each element via thin-film transistors directly located within matrix cells (pixels). However, these thin-film active matrices incorporated in a flexible or imperceptible form degrade the mechanical performance when a rigid silicon die is used as the driving circuit. In addition, the signals should be amplified at the nearest sensing points to enhance the signal-to-noise (S/N) ratio, as signals detected via sensors are weak. However, when signal amplifiers arranged on a rigid silicon die are used, the S/N ratio is deteriorated owing to long wiring between the outputs of sensors and the inputs of amplifiers.

Therefore, to ensure compatibility with flexible electronics concepts, the sensor array and respective electronic circuitry must both be imperceptible and integrated on the same flexible platform. For flexible electronic circuits, organic thin-film transistors (OTFTs) are potential candidates because they are intrinsically flexible and are compatible with low-cost printing processes that can be applied to large-area plastic substrates (*16*, *21*). In practice, fundamental logic and analog circuits, such as inverters and amplifiers, have been fabricated on the basis of OTFTs (*21*, *23*). Moreover, shift registers, which can be used as active-matrix drivers representing a square wave transfer circuit commonly composed of complementary thin-film transistors (TFTs), have also been fabricated on the basis of OTFTs (*24*–*29*).

[1]The Institute of Scientific and Industrial Research (ISIR), Osaka University, Mihogaoka 8-1, Ibaraki, Osaka 567-0047, Japan. [2]Graduate School of Engineering, Osaka University, 2-1 Yamadaoka, Suita, Osaka 565-0871, Japan. [3]National Institute of Advanced Industrial Science and Technology (AIST)–Osaka University Advanced Photonics and Biosensing Open Innovation Laboratory (PhotoBIO-OIL), 2-1 Yamadaoka, Suita, Osaka 565-0871, Japan. [4]Institute for Integrative Nanosciences, Leibniz Institute for Solid State and Materials Research Dresden (IFW Dresden), Helmholtzstraße 20, D-01069 Dresden, Germany. [5]Material Systems for Nanoelectronics, Chemnitz University of Technology, Reichenhainer Str. 70, D-09107 Chemnitz, Germany. [6]Research Center for Materials, Architectures and Integration of Nanomembranes (MAIN), Chemnitz University of Technology, Rosenbergstr. 6, D-09126 Chemnitz, Germany.
*Present address: Bundesanstalt für Materialforschung und -prüfung (BAM), Department for Non-Destructive Testing, Unter den Eichen 87, D-12205 Berlin, Germany.
†Corresponding author. Email: o.schmidt@ifw-dresden.de (O.G.S.); sekitani@sanken.osaka-u.ac.jp (T.S.)

However, complementary OTFTs exhibit severe problems that limit their application to shift registers as active-matrix drivers. Large-sized sensor arrays consume substantial power, leading to short operating times when autonomously powered by state-of-the-art flexible energy supplies (*30*). In other words, these energy sources set strict voltage and power supply constraints to the entire sensor system. Although shift registers composed of complementary OTFTs have been reported (*24*–*29*), the operating voltage or power consumption of one of the transistor species is still high. On the other hand, some researchers have recently reported complementary OTFT circuits with low-voltage operation or low power consumption based on n-type OTFTs with high performance (*31*–*33*). This progress is promising for complementary OTFTs circuits. However, the selectivity of these n-type OTFTs with high performance is still limited. The performance of most types of conventional n-type OTFTs is inferior to that of p-type OTFTs. In contrast, many p-type OTFTs with high performance have been reported. In addition, the reliability of these p-type OTFTs is higher than that of n-type OTFTs. Thus, a circuit configuration relying exclusively on p-type OTFTs is still preferred for organic shift register. Moreover, unipolar circuit designs have additional merit of a simpler fabrication process compared with complementary configurations. In practice, organic shift registers relying exclusively on p-type OTFTs have demonstrated high-speed or low-voltage operation. However, organic shift registers relying exclusively on p-type OTFTs cause high power consumption and output signal degradation owing to inadequate signal gain and/or distribution of carrier mobility and threshold voltages across all individual organic OTFTs (*34*–*38*).

This paper reports the development and low-voltage operation of an imperceptible organic electronic system based on only p-type OTFTs capable of integrating all components necessary for operation of an active magnetosensory matrix (MSM) system. The proposed MSM system comprises large thin-film magnetoresistive sensors and electronics based on p-type OTFT switches, bootstrap shift registers as active-matrix driver, and signal amplifiers (Fig. 1A). The components used in this work were fabricated on and integrated into the same imperceptible platform. The presence of an ultrathin polymer substrate and encapsulation facilitates the wearability of the magnetosensitive electronic membrane, as illustrated in Fig. 1B. It has been reported that imperceptible electronic elements demonstrated excellent mechanical stability under severe loading scenarios, such as bending, wrinkling, and crumpling (*39*). As explained in subsequent sections, OTFTs and magnetic sensors also have high compliance characteristics, as shown in Fig. 1C; it can be observed that the OTFTs and magnetic sensors are folded around a thin copper wire and bended, respectively (Fig. 1C), without affecting the electric performance. In addition to the integration of OTFT circuits with a magnetic sensor matrix, the development of this system involved overcoming several challenges associated with manufacturing technologies and organic circuit design via the exclusive use of p-type OTFTs to facilitate low-power high-speed operation while integrating a large number of elements within the array. To ensure exclusive use of p-type OTFTs, we designed an organic bootstrap shift register based on p-type OTFTs to address the problems of unipolar shift registers such as low-voltage operation, low power consumption, and output signal degradation.

RESULTS

Design of proposed imperceptible active MSM

The design and development of the proposed imperceptible MSM system were based on the circuit diagram depicted in Fig. 2A. A magnified view of the overall MSM system is depicted in Fig. 2B. As can be observed, the MSM system is equipped with a 3 × 6 array of giant magnetoresistance (GMR) sensors including redundancy. As depicted in Fig. 2C, all electronic units necessary for the acquisition, addressing, and conditioning of GMR signals were arranged on a single, entirely imperceptible platform requiring only three wires,

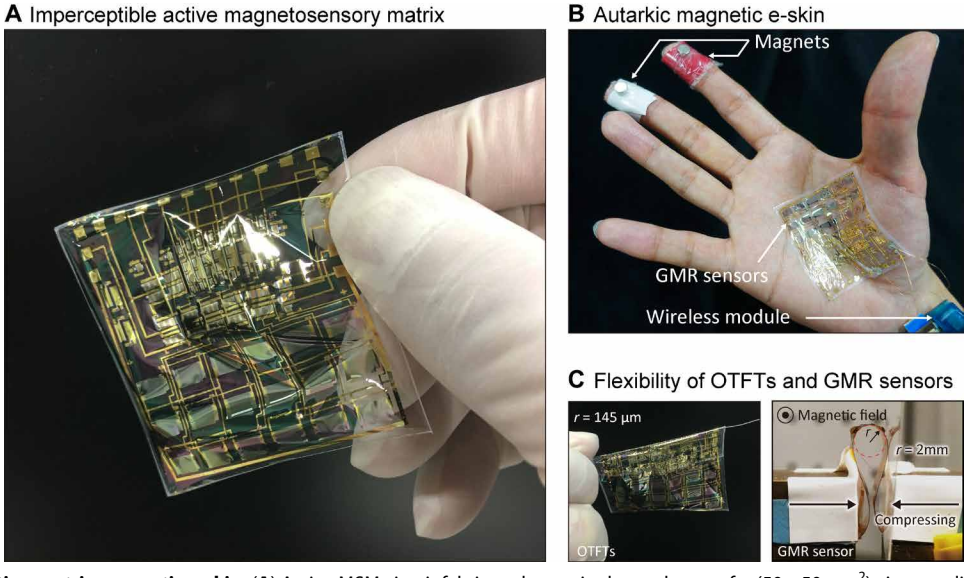

Fig. 1. Imperceptible active-matrix magnetic e-skin. (**A**) Active MSM circuit fabricated on a single parylene wafer (50 × 50 mm^2) via monolithic microfabrication on a 1.5-μm-thick substrate. (**B**) Demonstration of autarkic magnetic e-skin attached to human skin, facilitating position detection of fingers equipped with permanent magnets when approaching the palm. The device exhibits soft adhesion with a small amount of moisture in the palm. (**C**) Demonstration of robustness of OTFTs and giant magnetoresistance (GMR) sensors when bent to a radius of 145 μm and 2 mm, respectively (photo credit: Masaya Kondo, ISIR, Osaka University, PhotoBIO-OIL).

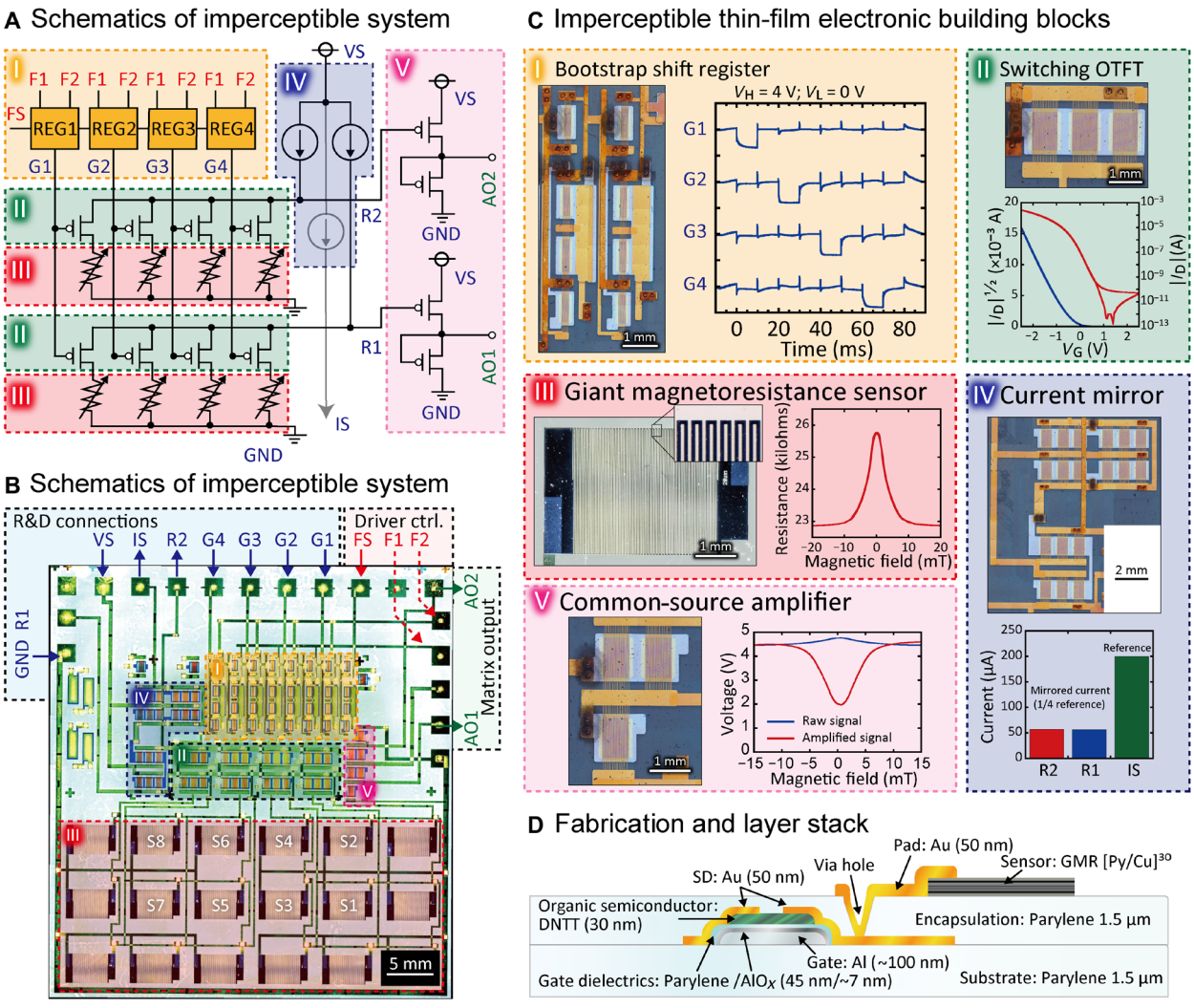

Fig. 2. Construction of the imperceptible magnetosensory system. (**A**) Schematic illustration of the five main circuit blocks of the MSM system. (**B**) Top view of the imperceptible magnetosensory system with an area of 50 × 50 mm^2 and comprising organic [dinaphtho[2,3-b:2′,3′-f]thieno[3,2-b]thiophene (DNTT)] electronic circuit and GMR sensors. (**C**) Separate micrographs for five main building blocks designed and implemented in imperceptible form along with corresponding main characteristics. (I) Optical micrograph of two stages of bootstrap shift register and typical output. (II) Optical micrograph of a switching OTFT and typical transfer curve. (III) Micrograph of a GMR sensor and typical transfer curve. (IV) Optical micrograph of a current mirror (top) and typical output current (bottom). The green bar shows the reference current, whereas the red and blue bars show the mirrored current from the reference. (V) Optical micrograph of a common-source amplifier and typical dc output signal from magnetic sensor. The blue curve shows the raw signal, whereas the red curve shows the amplified signal by the amplifier. (**D**) Cross-sectional schematic illustrating layered structure of imperceptible magnetosensory system (photo credit: Masaya Kondo, ISIR, Osaka University, PhotoBIO-OIL).

namely, FS, F1, and F2, for driving the active matrix (Fig. 2, A and B), except for the indispensable power supply and GND, as circuit (VS, IS, and GND). All functional components were integrated on a single polymer membrane with a thickness of approximately 3 µm, which is based on a multilevel thin-film architecture (refer to the cross-sectional schematic depicted in Fig. 2D), thereby retaining the key mechanical properties of imperceptible electronics (*39*).

As depicted in Fig. 2, the proposed MSM system comprises five major building blocks: (I) eight-stage bootstrap organic shift register to drive switching OTFTs, (II) switching matrix transistors for commutating each sensor cell, (III) GMR sensor array, (IV) current mirrors providing a stable bias current to each matrix row, and (V) organic inverters in the form of common-source amplifiers. The active matrix comprises two rows [R1 and R2 (AO1 and AO2)] and four columns (G1 to G4). Four magnetic sensor cells comprising switching OTFTs were connected to each row, whereas columns with transistor gates (G1 to G4) were driven by the shift register, as illustrated in Fig. 2A. Only a single column-gate terminal of switching OTFTs was enabled to simultaneously commutate corresponding sensor-cell voltages through each row line down to common-source row amplifiers. During sequential commutation, current mirrors were used to bias sensor cells via switching transistors in combination with shift registers that switched the gate state to ON. This resulted in a simple yet effective circuit design during operation as an active-matrix system.

The crucial functions of the active-matrix system are performed by implementing state-of-the-art OTFT technologies and magnetic sensors (*10*). In consideration of their excellent properties, such as

high electrical performance, low degradation, low specific weight, high flexibility, and good compliance with low-cost fabrication processes on large-sized substrates (*16*, *21*), dinaphtho[2,3-b:2′,3′-f]thieno[3,2-b]thiophene (DNTT)–based OTFTs were used to construct flexible circuits that constitute the MSM system. DNTT-based OTFTs can operate as p-type OTFTs. The OTFTs have a top-contact–bottom-gate structure, as depicted in Fig. 2D. An ultrathin (45-nm-thick) layer of parylene was used as the gate dielectric to facilitate low-voltage operation of circuits while achieving high yield and superior flexibility. The OTFTs with parylene gate dielectrics and DNTT active layers enabled the entire system to operate within 4 V.

Moreover, the use of a bootstrap circuit (*40*) was considered in this study to ensure the exclusive use of p-type OTFTs and facilitate effective low-power operation of the MSM system. However, despite several advantages offered by bootstrap circuits such as low power consumption, high operating speed, and tolerance to transistor parameter distribution, the available circuit designs are incompatible with p-type transistors, as they are primarily conceptualized for use with n-type transistors, such as high-quality n-type silicon. Although the development of other types of organic shift registers has been previously reported (*24*–*29*, *34*–*38*), bootstrap organic shift registers have not yet been demonstrated, based on neither n-type nor p-type OTFTs. In this study, a bootstrap shift register based on OTFTs was incorporated within the matrix to handle relevant sensor columns triggered by alternate clocking signals (F1 and F2) and the frame-start (FS) signal. The bootstrap shift register enabled the authors to exclusively use p-type OTFTs to build complex high-speed logics with low power consumption and negligible signal degradation (*40*).

Bootstrap shift register

Shift registers are essential electronic components that facilitate sequential addressing of element arrays while minimizing the number of external electric connections. A micrograph of two stages of the shift register used in the proposed MSM system is depicted in Fig. 2C (I) (left panel). The function of the shift register is simple. It propagates an ON voltage level across the gate columns of corresponding switching OTFTs within the sensor matrix. This is depicted in the right panel of Fig. 2C (I). The shift register may comprise many stages to facilitate operation of large active matrices while the number of control signal lines remains rather small. In the proposed system, the shift register requires only three control signals, namely, FS, F1, and F2, as mentioned earlier.

In this study, the authors conceptualized, designed, and fabricated an eight-stage organic bootstrap shift register circuit (see Fig. 3A) compatible with exclusive p-type OTFTs. The circuit has two repeating stages, as depicted in Fig. 3B, and comprises four p-type OTFTs (T1 to T4) and one metal-insulator-metal capacitor (C_{bst}) within each stage. The proposed design of the circuit did not require additional power connections, such as supply and ground (VS and GND), during operation; instead, clocking signals (F1 and F2) were used for this purpose. In the proposed design, the number of stages was doubled to facilitate utilization of every alternate stage for addressing column-OTFT gates within the matrix. In addition, the stages were incorporated to keep the phases of the control signals constant during sensor-readout sequences and demonstrate the potential for driving larger matrices using each stage for commutation of switching transistors.

A schematic clocking diagram of the first two stages is depicted in Fig. 3C to illustrate the operation of the bootstrap shift register. The working mechanism is presented in the "Operation of bootstrap shift register" section in Materials and Methods. Three square wave signals, namely, frame start (FS) and the first (F1) and second (F2) frame-shifting clocks, are required for the operation of the bootstrap circuit. These signals are supplied by synchronized wave function generators driving the bootstrap organic shift register. The key mechanism in the operation is that the stored potential in C_{bst} boosts the IN potential to nearly twice its original magnitude, as shown in Fig. 3C. The effective doubling of the potential oversaturates the connected OTFTs, thereby canceling any impact of OTFT parameter distribution. As well as Fig. 3C, the practical clocking diagram of the shift register (Fig. 3D) clearly demonstrates the operation of the circuit for all eight stages, including the voltage boost in IN lines, ON-state shifting across gate lines upon the arrival of each clock signal, and opening of the corresponding switching OTFTs within the matrix.

Figure 3E illustrates the relationship between the operating frequency and the input voltage of the shift register. The normalized output signal of the shift register $[(V_{OUT} - V_L)/(V_H - V_L)]$ was evaluated to define the operational frequency using variables V_{OUT}, V_H, and V_L, which represent the out-, high-, and low-voltage levels, respectively. The maximum operating frequency was defined as that at which the normalized output signal falls below 0.95. On the basis of this definition, the maximum operating frequencies were observed to be 100 and 50 Hz, respectively, when $V_H = 4$ and 3 V. The operating frequency of the bootstrap organic shift register can be determined in terms of the driving capability of the individual OTFT and C_{bst} capacitance, which can ultimately be reduced to the gate capacitance for OTFTs T1 and T3. Figure 3F depicts variations in the capacitance with respect to frequency for the eight capacitors present within the shift register. The change in capacitance is rather small, up to a frequency of 100 kHz. The capacitance of C_{bst} maintains a constant value of approximately 1.2 nF within the operating range (Fig. 3F) with almost no distribution, reflecting the high quality of the optimized fabrication technology.

The proposed circuit design does not require dc power supply since the power required by the circuit is provided by a two-phase clocking source, in which signals F1 and F2 alternately take on the role of ground and source terminals. In addition, the charge stored in the circuit does not dissipate completely, as is common in conventional bootstrap circuits (*40*); instead, it contributes to the next stage while requiring only half the power from F1 and F2 to charge the successive capacitor. Thus, the power dispersion could be notably lower than that of previously demonstrated organic shift registers (*24*–*29*, *34*–*38*). We estimated the power consumption in practice, as presented in table S1. The organic bootstrap shift register consumes approximately 0.8 nW and 0.23 μW of power per stage at static phase and a clocking frequency of 100 Hz, respectively. The estimation is explained in the "Static and dynamic power consumptions of bootstrap organic shift register" section in Materials and Methods.

Moreover, the bootstrapped shift register could be more reliable compared with other unipolar counterparts because the distribution of the mobility and threshold voltage of the individual OTFT does not play any role during the operation of the proposed circuit, as OTFTs T1 and T3 are always overdriven at higher voltages compared with the clocking voltage. Figure 3G depicts histograms of key OTFT performance parameters. The reproducibility and fabrication of the very basic functional elements of the proposed MSM system are accounted for. Statistical data concerning OTFT field-effect mobility

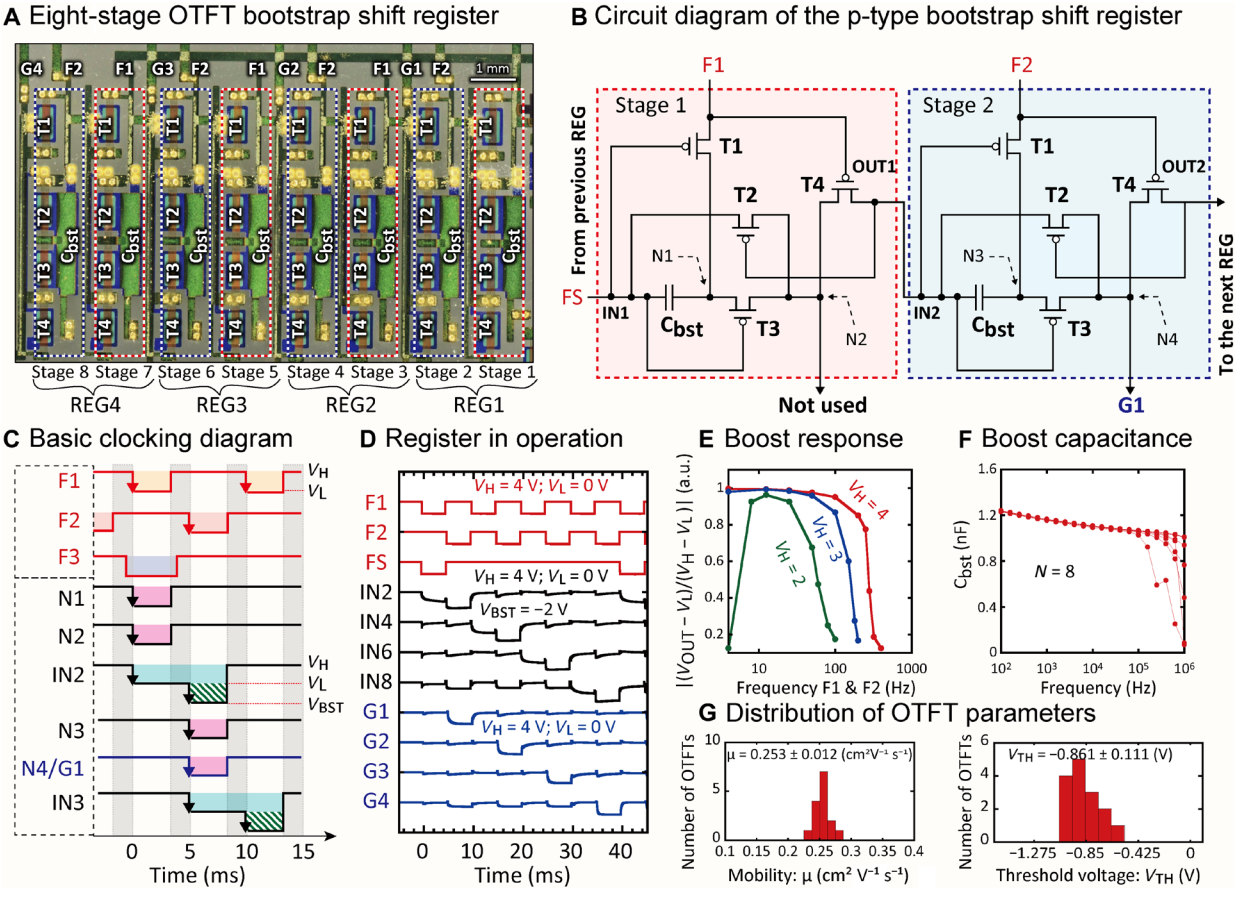

Fig. 3. Proposed organic bootstrap shift register and its performance. (**A**) Closeup of the eight stages of bootstrap shift register. (**B**) Circuit diagram representing the first two stages of the shift register. (**C**) Basic clocking diagram illustrating the correct function of driving signals for the first two stages, including the main clock (F1 and F2) and frame-start (FS) signals. (**D**) Typical timing diagram demonstrating the correct operation of the proposed eight-stage p-type imperceptible bootstrap shift register. The inputs F1, F2, and FS have two potentials as high level (V_H = 4 V) and low level (V_L = 0 V). In addition to V_H and V_L, the propagated IN signals have a lower potential (V_{BST} = −2 V) than V_L owing to bootstrap operation. (**E**) Boost response graph showing operating speed, which depends on the amplitudes of F1 and F2 signals that determine the charge-discharge cycle of boost capacitance. We applied three different V_H levels (V_H = 4, 3, and 2 V) to F1, F2, and FS. The perpendicular axis is the shift register output normalized by the difference between V_H and V_L (0 V) levels of FS. (**F**) Frequency response of eight boost capacitors revealing approximately a constant value of 1.2 nF at operating clock speed. (**G**) Distribution of OTFT parameters, such as mobility and threshold voltages, that do not affect shift register operation (photo credit: Masaya Kondo, ISIR, Osaka University, PhotoBIO-OIL).

and threshold voltage originate from 15 individual transistors and reveal an average mobility of μ = 0.253 $cm^2 V^{-1} s^{-1}$ with a standard deviation (SD) of 0.012 $cm^2 V^{-1} s^{-1}$ as well as an average threshold voltage of V_{TH} = −0.861 V with an SD of 0.111 V. Although these characteristics have relatively small dispersion, the variation is not negligible. However, the bootstrap shift register shows stable operation and a clear commutation of signals.

Switching transistors

Figure 2C (II) depicts the micrograph of a switching OTFT within the sensor matrix along with a typical transfer curve. In addition, fig. S1 (A and B) depicts the transfer characteristics of the 15 OTFTs and typical output characteristics, respectively. In the proposed MSM system, the OTFTs operate at gate (V_G) and drain (V_D) voltages in the range of 2.5 to −2.5 V and 0 to −2.5 V, respectively. The output characteristics demonstrate good linearity in the low V_D region, indicating the presence of ohmic contacts between the DNTT organic semiconductor and Au source/drain electrodes. OTFTs, therefore, demonstrate good saturation behavior when operating in the high V_D region. Figure S1C depicts the transfer characteristics of one of the switching OTFTs before and after its bending to different radii and crumpling, respectively (see Fig. 1C). The figures reveal no difference in the gate leakage current in either case. The effect of applied deformations was observed to be in the picoampere range, with corresponding transfer curves being nearly coincident. These results indicate that the OTFTs with the 45-nm-thick parylene gate insulator have high mechanical durability and are suitable for electronic components for imperceptible sensor system.

Magnetic sensors

In this study, GMR multilayers made of Py, that is, $Ni_{81}Fe_{19}$, a soft magnetic permalloy, and Cu, were considered for the fabrication of magnetic sensor cells. To adapt the basic electronic properties of sensor cells to OTFT requirements for efficient signal acquisition, we patterned GMR elements into a fine meander shape with a branch width of 20 μm and total footprint measuring 4 × 5 mm^2. Micrographs of individual meander-patterned GMR sensor cells are depicted in Fig. 2C (III). The sensor resistance was set in the range of 20 to

25 kilohms to satisfy the design requirements of prescribed resistance values of switching OTFTs. In practice, a narrow dispersion in the saturation resistance (R_{sat} = 22.5 ± 1.7 kilohms) and GMR ratio (r_{GMR} = 11.7 ± 0.5%) was observed in this study using nine different batches of GMR sensors, as depicted in fig. S2 (A and B). The selected Py/Cu GMR multilayers demonstrated high sensitivity when operating under conditions corresponding to low flux density values of the order of a few microteslas. A representative GMR curve of a single meander sensor cell is depicted in Fig. 2C (III). The total GMR ratio (i.e., change in resistance upon the application of an external magnetic field) was observed to be of the order of 10 to 13%. The proposed GMR sensor type has previously been proposed for use in the fabrication of imperceptible magnetoelectronic devices owing to its excellent stability during on-skin operation and resistance to severe deformations, including those induced by stretching (*10*). Although the MSM driving circuit was designed to read out eight (2 × 4) GMR sensor cells, a larger array of sensors (3 × 6 in total) was included in the system for redundancy [see Fig. 2B (red frame)]. Upon completion of the final circuit layout, appropriate GMR meander elements were selected for operation, and redundant units were intentionally destroyed.

To evaluate the performance of flexible GMR sensors, we fabricated separated elements with the same meander structure on a 1.5-μm-thick parylene film, as depicted in fig. S2C. A cross-sectional image of Py/Cu multilayers obtained using transmission electron microscopy is depicted in fig. S2D. Subsequent to their fabrication, the GMR sensor elements were subjected to bending tests, as depicted in Fig. 1C, to demonstrate their flexibility. During the bending tests, the GMR multilayer membrane was attached on a supporting Kapton film, and its magnetoresistance was measured in both the flat state and when it was bent in situ over a 2-mm radius, as depicted in fig. S2E. A comparison of the two cases indicates that the observed deviation in the measured magnetoresistance of the GMR multilayer membrane was less than 1%. This indicates that meander-shaped GMR sensors fabricated on an ultrathin parylene membrane are suitable for use in flexible electronics. Although the bending radius was limited to 2 mm in the bending tests described above, a previous study (*10*) conducted by the authors revealed that Py/Cu GMR multilayers fabricated on a similar polymeric membrane can withstand acute bending to radii of the order of a few micrometers. To verify the flexibility and the image of the imperceptible magnetic sensor, we demonstrated finger motion sensing based on flexible GMR sensors, as shown in fig. S3 and movie S1.

Current mirror

In the proposed circuit, a current source and a multichannel current mirror were integrated on the same substrate, as each magnetic sensor within the MSM system requires a stable supply current. During scanning cycles of the shift register, the current from mirror circuits was commutated through an active matrix to a particular sensor, and the observed voltage drop across the magnetic sensors was commutated back to common-source amplifiers. All current mirrors were fabricated from identical OTFTs with their drains and sources connected to respective matrix rows and VS. Magnified views of the current mirror micrographs are depicted in Fig. 2C (IV) and fig. S4A, whereas fig. S4B depicts a schematic with indicated line labels and OTFTs. The gates of all the OTFTs (T1 to T6) were connected to each other, where the reference was made out of four equivalent OTFTs (T1 to T4) and the mirror was made out of one OTFT (T5 or T6) (see fig. S4B). In other words, 0.25 times lower current than the defined current (IS) was used in the sensor circuits. This suppresses the variation effect of OTFTs, leading to stable and consistent current mirror. In this work, we used a 200-μA bias current as IS. In practice, the mirrored current is approximately 50 μA, and the variation is negligible, as shown in Fig. 2C (IV). The influence of individual currents on sensor responses of different rows can, if necessary, be calibrated and homogenized in the final application since they remain constant.

Organic common-source amplifiers

As discussed in the previous subsection, the voltage drop across magnetic sensors in the proposed system is commutated back as input to two common-source amplifiers through switching OTFTs. These inputs are directly connected to the output of row lines [see Fig. 2 (A and C), V]. The high amplification coefficient of these devices facilitates rail-to-rail operation of sensor matrices without the need for any external component for postprocessing of sensor information, thereby allowing for direct signal digitization and high S/N ratio. A zero-bias inverter is a simple and efficient circuit that operates as a common-source amplifier with high output gain. A magnified view of an amplifier channel with labeled interconnections is depicted in Fig. 4A, whereas the corresponding schematic is shown in Fig. 4B. The amplifier response is depicted in Fig. 4C, demonstrating excellent voltage transfer characteristics and corresponding gain. The proposed inverter circuit attained a gain of 87.5 at a supply voltage of 3 V.

To visualize the effect of the common-source amplifiers on the magnetic sensor response, we compared the amplified signal characteristics of one GMR sensor (AO1 and AO2) with those of a raw signal without amplification (R1 and R2), as depicted in Fig. 4D, for two positions of magnet approaching different magnetic sensor cells correspondingly marked in red and blue circles in the figure. In this demonstration, strong NdFeB magnets were used. Both sensor cells were connected to the same word line, and both bit lines were connected to organic amplifiers. Raw and amplified signals for both sensor cells (red and blue) were plotted in corresponding colors (Fig. 4D) under conditions in which the magnets repeatedly approached the two cells. As observed in the figure, the raw signals, which initially measured approximately 100 mV, were amplified to output signals measuring several volts. This extended voltage capability enables direct signal digitization, setting a range of voltage levels to control other systems using the proposed device. Without amplification, the output voltages of the sensor cells were observed to be small, making it difficult to recognize the presence of a magnetic field or even the position of its magnetic source. With amplification, however, the adjacent sensor cell being approached by the permanent magnet can be easily distinguished. This is the first demonstration of signal amplification using an ultraflexible MSM system equipped with organic amplifiers.

Two-dimensional mapping using active MSM

Real-time two-dimensional mapping of magnetic fields using the proposed imperceptible MSM system driven by a bootstrap organic shift register is described in this section. The mapping functionality accomplishes a key task of distributed magnetic sensor networks, thereby facilitating their utilization in applications such as magnetic e-skins. In this study, eight GMR sensors (indicated by the dotted red box in Fig. 5A) were selected from within the sensor matrix, and

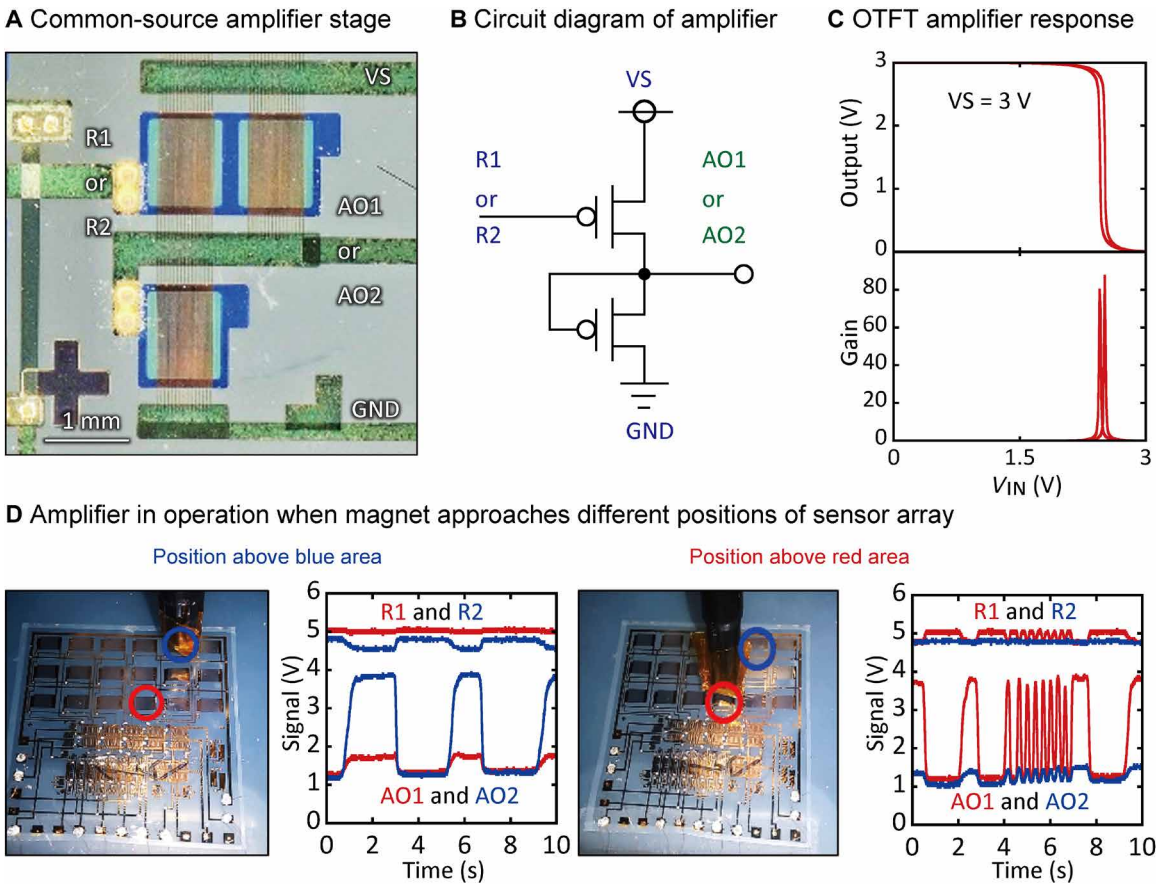

Fig. 4. Proposed common-source amplifier layout and its performance. (**A**) Magnified view of a common-source amplifier. (**B**) Circuit diagram representing one stage of a common-source amplifier. (**C**) Response of OTFT common-source amplifier with voltage transfer and gain characteristics. (**D**) Demonstration of common-source amplifier in operation in which signals from two sensors within the blue and red circles were recorded on row lines R1 and R2 and amplifier outputs AO1 and AO2 when corresponding sensor locations were approached by a strong NdFeB permanent magnet. The maximum magnetic field of the magnet is more than 500 mT (photo credit: Daniil Karnaushenko, IFW Dresden).

a weak ferrite permanent magnet was placed at different locations close to the sensor matrix to realize two-dimensional magnetic field mapping. Labels on each sensor cell indicate the corresponding column gate (G) and row (R) addresses within the driving circuit. Figure 5B depicts the time history of sequential driving signals generated by the clocked shift register on each column gate line (G1 to G4). These signals successively activate respective switching OTFTs (highlighted by green box in Fig. 5A). The acquired signals on both row lines, as observed upon sensor cell activation, are plotted in Fig. 5B. As can be observed, the voltage levels on row lines differ from those of driving signals on column gate lines. Mapping of the magnetic field can be accomplished on the basis of this difference in the voltage levels between the column gate and row lines, as shown in the column bar charts in Fig. 5C. The observed trend in the variations of the magnetic field intensity detected by each sensor cell is in good agreement with that of variations in the magnet position, as depicted in Fig. 5A. It was also observed that the sensor matrix accurately maps the magnetic fields for three different magnet positions. The mapping feature can, therefore, be used to track the positions of magnetic objects in the three-dimensional environment surrounding the sensor matrix by considering the magnetic flux readings obtained from sensors. This is the first demonstration of an active MSM system driven by a bootstrap organic shift register.

DISCUSSION

This paper reported the development of an imperceptible magnetic sensor matrix organic system comprising 2 × 4 GMR sensors, bootstrap organic shift register, and organic amplifiers on the same flexible platform. In addition to the full system integration, we addressed the challenges in the OTFT system, that is, low-voltage operation and the exclusive utilization of p-type OTFTs. In the proposed system, the magnetic sensor matrix was demonstrated to be driven by an organic bootstrap shift register. In addition, the amplification of detected signals was accomplished using organic amplifiers. The use of p-type OTFT–based bootstrap shift registers with excellent electrical performance, high operating speed, and low driving voltage (less than 4 V) was successfully demonstrated. It was observed that the static power consumption of the proposed system (approximately 0.8 nW) is lower compared with that of conventional designs. In addition, the dynamic power consumption of the proposed system (approximately 0.23 μW) is also lower compared with the standby power dissipation of other existing systems (refer to table S1 and Materials and Methods).

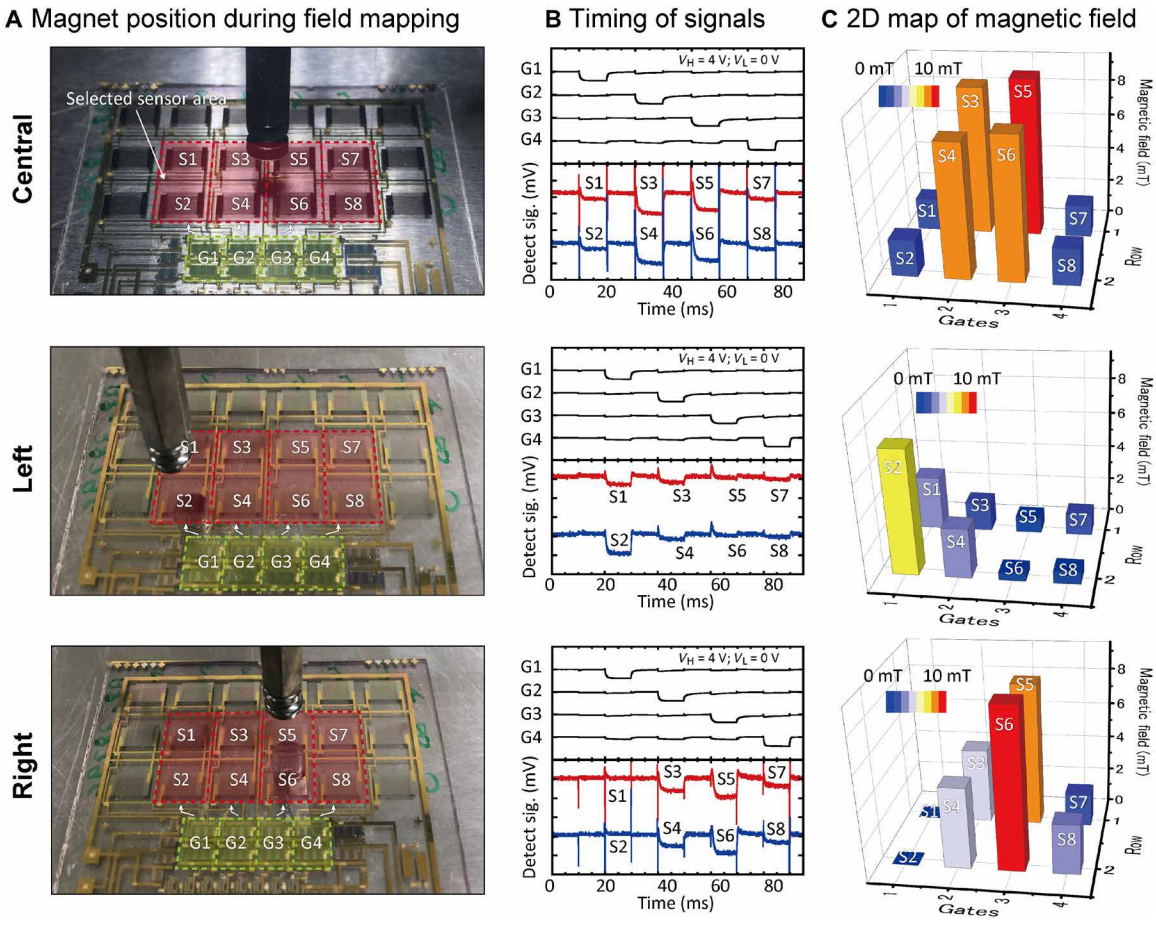

Fig. 5. Demonstration of two-dimensional mapping of magnetic field. (**A**) Detection of magnetic field using a weak ferrite permanent magnet placed at various positions within the sensor matrix. The maximum magnetic field of the magnet is approximately 40 mT. (**B**) Signals of sensor matrix scanned using bootstrap organic shift register and variations in row line voltage as sensor matrix is scanned with the respective magnet position, shown in (A). The detected signal lines have an offset voltage of 150 mV. (**C**) Two-dimensional (2D) map of applied magnetic field (photo credit: Masaya Kondo, ISIR, Osaka University, PhotoBIO-OIL).

This reduced power consumption was primarily facilitated by the bootstrap shift register design in which only the active stage consumes the power required for charging the boost capacitor, suppressing dc power losses. Hence, static power dissipation in the proposed system depends exclusively on current leaking from gate terminals of switching transistors. High-speed operation and ultralow power consumption of the proposed circuit make it particularly attractive for use as a flexible and imperceptible system. The integration of flexible low operating voltage GMR sensors with highly reliable OTFTs, therefore, facilitates realization of an imperceptible, wearable, and autonomous battery-powered system. The MSM system described here represents a high level of complexity and functionalization in terms of system integration for use in imperceptible electronic platforms. The system has additionally been demonstrated to be capable of accurately mapping magnetic fields in two dimensions with high precision. The inclusion of a word line scanner and common-source amplifier, the ability to work at low supply voltages below 4 V, and high-frequency operation at approximately 100 Hz make this system the most imperceptible and functional design to date. The authors believe that this study would pave the way for the development of a new generation of flexible electronics to be used in applications such as e-skins, soft robotics, and biomedical science.

MATERIALS AND METHODS

Design of ultraflexible magnetic sensor matrix

The HSPICE software package (Synopsys Inc., USA) was used to simulate and design the eight-stage bootstrap organic shift register and to define the parameter values of the magnetic sensor matrix. In addition, Level 61 PRI, an Si-based TFT model, was used to simulate the characteristics of switching OTFTs, and the corresponding channel length was initially set to 10 μm. The channel widths of the switching OTFTs and bootstrap organic shift registers were set to 96 and 12 mm, respectively, based on the simulation results. In terms of organic inverters, the size ratio of the driving OTFTs to the load OTFTs was set to 2:1. Last, the capacitance of bootstrap capacitors comprising the organic shift register circuit was set to approximately 1 nF.

Fabrication and characterization of OTFTs

A 100-nm-thick Al layer was first thermally evaporated onto a 1.5-μm-thick diX-SR (parylene) layer supported on a glass film using the shadow mask technique. The Al layer acted as the gate electrode, and its surface was subsequently treated with oxygen plasma at 100 W for 3 min before the deposition of parylene (45 nm thick) as the gate dielectric using chemical vapor deposition. DNTT and

Au layers (30 and 50 nm thick, respectively) were thermally deposited using the shadow mask technique to form the active layer and source and drain electrodes along with corresponding interconnections, respectively. After fabrication of OTFT circuits, the device was annealed in vacuum for 1 hour at 120°C and approximately 100-Pa vacuum pressure. Last, a 1.5-μm-thick parylene layer was deposited using chemical vapor deposition to facilitate device encapsulation. A laser ablation process (T-Centric Laser Marker, MD-T1000W; KEYENCE Co. Ltd.) was performed to drill contact holes for circuit interconnections between respective device layers. All electric characterizations were performed in ambient air in a dark room.

Fabrication and characterization of Py/Cu GMR multilayers

An ultraviolet lithography lift-off process was performed using a positive AZ 5214E image reversal resist (AZ Electronic Materials, Luxembourg) and a Karl Suss MA56 mask aligner (SÜSS MicroTec SE, Germany) to define individual meander patterns on top of the driving circuit architecture and respective interconnection structures. Subsequently, Py (1.5 nm) or [Py (1.5 nm)/Cu (2.3 nm)]^{30} GMR multilayers antiferromagnetically coupled in the second maximum were grown using magnetron sputtering deposition at room temperature. The values of the base pressure, Ar sputter pressure, and deposition rate were set to 7.0×10^{-7} mbar, 7.5×10^{-4} mbar, and 2 Å/s, respectively. The Py/Cu GMR meanders with 20-μm-wide branches running along the short axis of a 4×5 mm^2 rectangular area were completed after the lift-off process. The sizes and shapes of the individual GMR sensor cells were selected to obtain resistance values in the range of 20 to 25 kilohms, as defined by the initial system simulation. In terms of characterization, four-point probe measurements were conducted in a dc probe station using an integrated electromagnet to facilitate application of an in-plane magnetic field along the main trenches of the meander structure. Bending tests were conducted on the imperceptible GMR meander using an in-house bending test setup intended for in situ magnetoelectric characterization.

Operation of bootstrap shift register

As depicted in Fig. 3C, signals F1 and F2 must exist in opposite phases and be separated by a temporal gap. The FS signal must overlap the gap between F1 and F2 (gray regions in Fig. 3C). Once the input signal (IN) is negative and determined to be small compared with the threshold voltage of OTFTs, OTFT T1 becomes open, and signals F1 or F2 can be transferred to nodes N1, N3, etc. When either F1 or F2 equals 0 V, the corresponding nodes operate as temporal ground, and capacitor C_{bst} charges up to the potential $V_H - V_L$. When IN has a high-impedance state (i.e., OTFT T4 is closed), the charge within C_{bst} is stored for some time, during which T1 and T3 remain open. When the phase of either F1 or F2 changes along with an increase in negative voltage, nodes N1, N3, etc. follow the potential stored in C_{bst} owing to T1 being open. This, in turn, boosts the IN potential to nearly twice its original magnitude. As the gate-source voltage for T3 is equivalent to that across C_{bst}, the OTFT effectively transfers the voltage of F1 or F2 to nodes N2, N4, etc., thereby switching the gates of switching OTFTs to the ON state without any voltage degradation. The effective doubling of the T3 gate voltage oversaturates the transistor, thereby canceling any impact of OTFT parameter distribution. In the bootstrap circuit, OTFT T2 is required for final discharge of the boost capacitor when the IN signal for the next stage is set to ON potential. This marks the completion of one shift cycle.

Static and dynamic power consumptions of bootstrap organic shift register

The static power consumption of the bootstrap circuit was first estimated. As mentioned here, the bootstrap shift register itself does not require an external dc power supply and ground. In other words, the circuit produces no leakage current passing directly through the dc power supply to ground. Hence, its static power consumption is low compared with that of conventional shift registers. The static power consumption is mainly defined on the basis of leakage currents from the gate terminals of switching OTFTs connected to the shift register output. Thus, for accurate estimation of the static power consumption, the measured OTFT gate leakage current value of 0.2 nA was used in this study. Consequently, the static power consumption per stage of the bootstrap organic shift register was calculated to be 0.8 nW based on an operating voltage of 4 V. In contrast, the dynamic power consumption of the bootstrap shift register was considered to be given by $C_G V_{CLK}^2 f$, where C_G denotes the load capacitance, V_{CLK} denotes the clock voltage, and f denotes the clock frequency (*40*). The value of the parameter C_G corresponds approximately to the total gate capacitance of 2 OTFTs (73 pF/OTFT) composed of the shift register. Considering the effect of 2 switching OTFTs (585 pF/OTFT) connected to the output of the bootstrap shift register, the capacitance is also added. Therefore, for the case where $V_{CLK} = 4$ V and $f = 100$ Hz, the dynamic power consumption of the organic shift register was observed to be 0.23 μW. Considering switching OTFTs, the total dynamic power consumption was approximately observed to be 0.23 + 1.9 = 2.13 μW.

Two-dimensional mapping of magnetic field by bootstrap organic shift register

To facilitate operation of the bootstrap organic shift register, square wave input signals were applied at terminals F1 and F2 (high level, 4 V; low level, 0 V), and three different operating frequencies of 12.5, 50.0, and 100 Hz were considered. The input signals were supplied using synchronized function generators, and all measurements were carried out on a supporting glass structure. A ferrite permanent magnet that produces a very weak magnetic field compared with that of NdFeB magnets was used in this demonstration. In Fig. 5 (B and C), the output voltage signals were transformed to magnetic field values based on precalibrations between each sensor output voltage and the magnetic field measured using a magnetometer as reference. In the measurements, the magnet was fixed in the approximately same height.

SUPPLEMENTARY MATERIALS

Supplementary material for this article is available at http://advances.sciencemag.org/cgi/content/full/6/4/eaay6094/DC1

Fig. S1. Basic OTFT characteristics.
Fig. S2. Basic GMR characteristics.
Fig. S3. Autarkic operation of wireless magnetosensory e-skin.
Fig. S4. Configuration of current mirror.
Table S1. Comparison of characteristics of organic shift registers having various structures.
Movie S1. Demonstration of wireless finger motion sensing based on imperceptible magnetic sensors.

REFERENCES AND NOTES

1. S. Wang, J. Xu, W. Wang, G. J. N. Wang, R. Rastak, F. Molina-Lopez, J. W. Chung, S. Niu, V. R. Feig, J. Lopez, T. Lei, S. Kwon, Y. Kim, A. M. Foudeh, A. Ehrlich, A. Gasperini, Y. Y. Boris Murmann, J. B.-H. Tok, Z. Bao, Skin electronics from scalable fabrication of an intrinsically stretchable transistor array. *Nature* **555**, 83–88 (2018).
2. J. Park, M. Kim, Y. Lee, H. S. Lee, H. Ko, Fingertip skin–inspired microstructured ferroelectric skins discriminate static/dynamic pressure and temperature stimuli. *Sci. Adv.* **1**, e1500661 (2015).
3. T. Yokota, Y. Inoue, Y. Terakawa, J. Reeder, M. Kaltenbrunner, T. Ware, K. Yang, K. Mabuchi, T. Murakawa, M. Sekino, W. Voit, T. Sekitani, T. Someya, Ultraflexible,

large-area, physiological temperature sensors for multipoint measurements. *Proc. Natl. Acad. Sci. U.S.A.* **112**, 14533–14538 (2015).
4. S. Ota, A. Ando, D. Chiba, A flexible giant magnetoresistive device for sensing strain direction. *Nat. Electron.* **1**, 124–129 (2018).
5. N. Lu, C. Lu, S. Yang, J. Rogers, Highly sensitive skin-mountable strain gauges based entirely on elastomers. *Adv. Funct. Mater.* **22**, 4044–4050 (2012).
6. Y. Yamamoto, S. Harada, D. Yamamoto, W. Honda, T. Arie, S. Akita, K. Takei, Printed multifunctional flexible device with an integrated motion sensor for health care monitoring. *Sci. Adv.* **2**, e1601473 (2016).
7. N. Lu, D. H. Kim, Flexible and stretchable electronics paving the way for soft robotics. *Soft Robot.* **1**, 53–62 (2014).
8. T. Yokota, P. Zalar, M. Kaltenbrunner, H. Jinno, N. Matsuhisa, H. Kitanosako, Y. Tachibana, W. Yukita, M. Koizumi, T. Someya, Ultraflexible organic photonic skin. *Sci. Adv.* **2**, e1501856 (2016).
9. W. Gao, S. Emaminejad, H. Y. Y. Nyein, S. Challa, K. Chen, A. Peck, H. M. Fahad, H. Ota, H. Shiraki, D. Kiriya, D. H. Lien, G. A. Brooks, R. W. Davis, A. Javey, Fully integrated wearable sensor arrays for multiplexed in situ perspiration analysis. *Nature* **529**, 509–514 (2016).
10. M. Melzer, M. Kaltenbrunner, D. Makarov, D. Karnaushenko, D. Karnaushenko, T. Sekitani, T. Someya, O. G. Schmidt, Imperceptible magnetoelectronics. *Nat. Commun.* **6**, 6080 (2015).
11. M. Melzer, J. I. Mönch, D. Makarov, Y. Zabila, G. S. Cañón Bermúdez, D. Karnaushenko, S. Baunack, F. Bahr, C. Yan, M. Kaltenbrunner, O. G. Schmidt, Wearable magnetic field sensors for flexible electronics. *Adv. Mater.* **27**, 1274–1280 (2015).
12. G. S. Cañón Bermúdez, H. Fuchs, L. Bischoff, J. Fassbender, D. Makarov, Electronic-skin compasses for geomagnetic field-driven artificial magnetoreception and interactive electronics. *Nat. Electron.* **1**, 589–595 (2018).
13. G. S. Cañón Bermúdez, D. D. Karnaushenko, D. Karnaushenko, A. Lebanov, L. Bischoff, M. Kaltenbrunner, J. Fassbender, O. G. Schmidt, D. Makarov, Magnetosensitive e-skins with directional perception for augmented reality. *Sci. Adv.* **4**, eaao2623 (2018).
14. Y.-f. Chen, Y. Mei, R. Kaltofen, J. I. Mönch, J. Schumann, J. Freudenberger, H.-J. Klauß, O. G. Schmidt, Towards flexible magnetoelectronics: Buffer-enhanced and mechanically tunable GMR of Co/Cu multilayers on plastic substrates. *Adv. Mater.* **20**, 3224–3228 (2008).
15. C. Zysset, N. Münzenrieder, L. Petti, L. Büthe, G. A. Salvatore, G. Tröster, IGZO TFT-based all-enhancement operational amplifier bent to a radius of 5 mm. *IEEE Electron Device Lett.* **34**, 1394–1396 (2013).
16. M. Kaltenbrunner, T. Sekitani, J. Reeder, T. Yokota, K. Kuribara, T. Tokuhara, M. Drack, R. Schwödiauer, I. Graz, S. Bauer-Gogonea, S. Bauer, T. Someya, An ultra-lightweight design for imperceptible plastic electronics. *Nature* **499**, 458–463 (2013).
17. N. Matsuhisa, M. Kaltenbrunner, T. Yokota, H. Jinno, K. Kuribara, T. Sekitani, T. Someya, Printable elastic conductors with a high conductivity for electronic textile applications. *Nat. Commun.* **6**, 7461 (2015).
18. K. Tsukada, Y. Haga, K. Morita, N. Song, K. Sakai, T. Kiwa, W. Cheng, Detection of inner corrosion of steel construction using magnetic resistance sensor and magnetic spectroscopy analysis. *IEEE Trans. Magn.* **52**, 16104894 (2016).
19. G. A. Salvatore, N. Münzenrieder, C. Barraud, L. Petti, C. Zysset, L. Büthe, K. Ensslin, G. Tröster, Fabrication and transfer of flexible few-layers MoS_2 thin film transistors to any arbitrary substrate. *ACS Nano* **7**, 8809–8815 (2013).
20. G. A. Salvatore, N. Münzenrieder, T. Kinkeldei, L. Petti, C. Zysset, I. Strebel, L. Büthe, G. Tröster, Wafer-scale design of lightweight and transparent electronics that wraps around hairs. *Nat. Commun.* **5**, 2982 (2014).
21. T. Sekitani, T. Yokota, K. Kuribara, M. Kaltenbrunner, T. Fukushima, Y. Inoue, M. Sekino, T. Isoyama, Y. Abe, H. Onodera, T. Someya, Ultraflexible organic amplifier with biocompatible gel electrodes. *Nat. Commun.* **7**, 11425 (2016).
22. N. Münzenrieder, D. Karnaushenko, L. Petti, G. Cantarella, C. Vogt, L. Büthe, D. D. Karnaushenko, O. G. Schmidt, D. Makarov, G. Tröster, Entirely flexible on-site conditioned magnetic sensorics. *Adv. Electron. Mater.* **2**, 1600188 (2016).
23. H. Klauk, U. Zschieschang, J. Pflaum, M. Halik, Ultralow-power organic complementary circuits. *Nature* **445**, 745–748 (2007).
24. B. Crone, A. Dodabalapur, Y. Y. Lin, R. W. Filas, Z. Bao, A. LaDuca, R. Sarpeshkar, H. E. Katz, W. Li, Large-scale complementary integrated circuits based on organic transistors. *Nature* **403**, 521–523 (2000).
25. D. E. Schwartz, T. N. Ng, Comparison of static and dynamic printed organic shift registers. *IEEE Electron Device Lett.* **34**, 271–273 (2013).
26. M. Uno, N. Isahaya, B. Cha, M. Omori, A. Yamamura, H. Matsui, M. Kudo, Y. Tanaka, Y. Kanaoka, M. Ito, J. Takeya, High-yield, highly uniform solution-processed organic transistors integrated into flexible organic circuits. *Adv. Electron. Mater.* **3**, 1600410 (2017).
27. S. Abdinia, T.-H. Ke, M. Ameys, J. Li, S. Steudel, J. L. Vandersteen, B. Cobb, F. Torricelli, A. van Roermund, E. Cantatore, Organic CMOS line drivers on foil. *J. Disp. Technol.* **11**, 564–569 (2015).
28. B. K. Crone, A. Dodabalapur, R. Sarpeshkar, R. W. Filas, Y.-Y. Lin, Z. Bao, J. H. O'Neill, W. Li, H. E. Katz, Design and fabrication of organic complementary circuits. *J. Appl. Phys.* **89**, 5125–5132 (2001).
29. T. N. Ng, D. E. Schwartz, L. L. Lavery, G. L. Whiting, B. Russo, B. Krusor, J. Veres, P. Broms, L. Herlogsson, N. Alam, O. Hagel, J. Nilsson, C. Karlsson, Scalable printed electronics: An organic decoder addressing ferroelectric non-volatile memory. *Sci. Rep.* **2**, 585 (2012).
30. M. Kaltenbrunner, M. S. White, E. D. Głowacki, T. Sekitani, T. Someya, N. S. Sariciftci, S. Bauer, Ultrathin and lightweight organic solar cells with high flexibility. *Nat. Commun.* **3**, 770 (2012).
31. T. H. Ke, R. Müller, B. Kam, M. Rockele, A. Chasin, K. Myny, S. Steudel, W. D. Oosterbaan, L. Lutsen, J. Genoe, L. Leuken, B. Putten, P. Heremans, Scaling down of organic complementary logic gates for compact logic on foil. *Org. Electron.* **15**, 1229–1234 (2014).
32. T.-H. Ke, K. Myny, A. Chasinin, R. Müller, P. Heremans, S. Steudel, in *2014 IEEE International Electron Devices Meeting* (IEEE, 2014), pp. 26.1.1–26.1.4; http://ieeexplore.ieee.org/document/7047110/.
33. U. Kraft, T. Zaki, F. Letzkus, J. N. Burghartz, E. Weber, B. Murmann, H. Klauk, Low-voltage, high-frequency organic transistors and unipolar and complementary ring oscillators on paper. *Adv. Electron. Mater.* **5**, 1800453 (2019).
34. D. Raiteri, P. van Lieshout, A. van Roermund, E. Cantatore, Positive-feedback level shifter logic for large-area electronics. *IEEE J. Solid-State Circuits* **49**, 524–535 (2014).
35. P. van Lieshout, E. van Veenendaalin, L. Schrijnemakers, G. Gelinck, F. Touwslager, E. Huitema, in *ISSCC. 2005 IEEE International Digest of Technical Papers. Solid-State Circuits Conference, 2005* (IEEE, 2005), vol. 79, pp. 578–580; http://ieeexplore.ieee.org/document/1494127/.
36. M. Elsobky, M. Elattar, G. Alavi, F. Letzkus, H. Richter, U. Zschieschang, M. Strecker, H. Klauk, J. N. Burghartz, A digital library for a flexible low-voltage organic thin-film transistor technology. *Org. Electron.* **50**, 491–498 (2017).
37. M. Elsobky, Y. Mahsereci, Z. Yu, H. Richter, J. N. Burghartz, J. Keck, H. Klauk, U. Zschieschang, Ultra-thin smart electronic skin based on hybrid system-in-foil concept combining three flexible electronics technologies. *Electron. Lett.* **54**, 338–340 (2018).
38. G. H. Gelinck, H. E. A. Huitema, E. van Veenendaal, E. Cantatore, L. Schrijnemakers, J. B. van der Putten, T. C. Geuns, M. Beenhakkers, J. B. Giesbers, B. H. Huisman, E. J. Meijer, E. M. Benito, F. J. Touwslager, A. W. Marsman, B. J. E. vanRens, D. M. de Leeuw, Flexible active-matrix displays and shift registers based on solution-processed organic transistors. *Nat. Mater.* **3**, 106–110 (2004).
39. M. Drack, I. Graz, T. Sekitani, T. Someya, M. Kaltenbrunner, S. Bauer, An imperceptible plastic electronic wrap. *Adv. Mater.* **27**, 34–40 (2015).
40. L. Lee, S. Al-Sarawi, D. Abbott, Dynamic bootstrapped shift register for smart sensor arrays. *Smart Mater. Struct.* **14**, 569–574 (2005).

Acknowledgments: We greatly appreciate the support extended by the Research Technology Department of the Leibniz IFW Dresden and the clean room team headed by R. Engelhardt (Leibniz IFW Dresden) during the development of the experimental setup used in this study. We thank C. Krien and I. Fiering (Leibniz IFW Dresden) for the deposition of metallic thin films. In addition, we thank D. D. Karnaushenko for the assistance provided during experimental work. **Funding:** This work was supported by JSPS KAKENHI grant numbers JP 18J12316 and 18H01861; the New Energy and Industrial Technology Development Organization (NEDO); the Center of Innovation Program from Japan Science and Technology Agency (JST); the Dynamic Alliance for Open Innovation Bridging Human, Environment and Materials from the Ministry of Education, Culture, Sports, Science and Technology of Japan (MEXT); the Research Program for Next Generation Young Scientists of "Five-star Alliance" in "NJRC Mater. & Dev."; and the Advanced Photonics and Biosensing Open Innovation Laboratory, National Institute of Advanced Industrial Science and Technology (AIST), the German Research Foundation DFG (Gottfried Wilhelm Leibniz Prize granted in 2018, FOR 1713, SCHM 1298/15-1&2 and KA5051/1-1), BMBF project Nanett (FKZ: 03IS2011F), and the Leibniz association via the Leibniz competition (J21/2017). **Author contributions:** M.K. developed the process for the fabrication of OTFT circuits for the sensor matrix. M.M. and D.K. designed and optimized the Py/Cu GMR multilayers used in the sensor matrix. M.K., M.A., and S.Y. carried out the design and circuit simulations. D.K., M.K., and S.Y. conceived the concept of the active bootstrap organic matrix. M.K. fabricated the device and conducted experiments to determine its characteristics, assisted by M.M., D.K., and T.U. M.K., assisted by T.U., T.A., Y.N., and D.K., created the video clip that demonstrates the use of the proposed system for finger motion sensing. M.K., M.M., and D.K. compiled this manuscript, assisted by T.U. and S.Y. T.S., O.G.S., and D.K. initiated and supervised the entire project. The manuscript has been reviewed by all authors. **Competing interests:** The authors declare that they have no competing interests. **Data and materials availability:** All data needed to evaluate the conclusions in the paper are present in the paper and/or the Supplementary Materials. Additional data related to this paper may be requested from the authors.

Submitted 3 July 2019
Accepted 25 November 2019
Published 22 January 2020
10.1126/sciadv.aay6094

Citation: M. Kondo, M. Melzer, D. Karnaushenko, T. Uemura, S. Yoshimoto, M. Akiyama, Y. Noda, T. Araki, O. G. Schmidt, T. Sekitani, Imperceptible magnetic sensor matrix system integrated with organic driver and amplifier circuits. *Sci. Adv.* **6**, eaay6094 (2020).

Imperceptible magnetic sensor matrix system integrated with organic driver and amplifier circuits

M. Kondo, M. Melzer, D. Karnaushenko, T. Uemura, S. Yoshimoto, M. Akiyama, Y. Noda, T. Araki, O. G. Schmidt and T. Sekitani

Sci Adv **6** (4), eaay6094.
DOI: 10.1126/sciadv.aay6094